

A Micro-Ellipsoid Model for Wet Porous Materials Rendering

GAOLE PAN, Nanjing University of Science and Technology, China

YUANG CUI*, Anhui Science and Technology University, China

JIAN YANG, Nanjing University of Science and Technology, China

BEIBEI WANG†, Nanjing University, China



Fig. 1. In this paper, we present a transmittable micro-ellipsoid model to render wet porous materials with physical parameters. It can produce vivid appearances on a wide range of materials. Examples include the wet cloths, flowerpots and sculptures as shown above.

Wet porous materials, like wet ground, moist walls, or wet cloth, are common in the real world. These materials consist of transmittable particles surrounded by liquid, where the individual particle is invisible in the macroscopic view. While modeling wet porous materials is critical for various applications, a physically based model for wet porous materials is still absent. In this paper, we model these appearances in the media domain by extending the anisotropic radiative transfer equation to model porosity and saturation. Then, we introduce a novel particle model- *micro-ellipsoid*- by treating each particle as a transmittable ellipsoid, analogous to a micro-flake, to statistically characterize the overall optical behavior of the medium. This way, the foundational theory for media with porosity and saturation is established. Building upon this new medium, we further propose a practical bidirectional scattering distribution function (BSDF) model within the position-free framework- *WetSpongeCake*. As a result, our *WetSpongeCake* model is able to represent various appearances of wet porous materials using physical parameters (e.g., porosity and saturation), allowing both reflection and transmission. We validated our model through several examples: a piece of wet cloth, sand saturated with different liquids, or damp sculptures, demonstrating its ability to match real-world appearances closely.

*Research done when Yuang Cui was an intern at Nanjing University of Science and Technology.

†Corresponding author.

Authors' addresses: Gaole Pan, Nanjing University of Science and Technology, China, pangaole@njust.edu.cn; Yuang Cui, Anhui Science and Technology University, China, yuangcui@outlook.com; Jian Yang, Nanjing University of Science and Technology, China, csjyang@njust.edu.cn; Beibei Wang, Nanjing University, China, beibei.wang@nju.edu.cn.

CCS Concepts: • **Computing methodologies** → **Rendering; Reflectance modeling**.

Additional Key Words and Phrases: wet porous materials, radiative transfer equation, micro-flake, BSDF, phase function

1 INTRODUCTION

Reproducing appearances from the real world with material models is essential in computer graphics. Material models for some common appearances (e.g., plastic, metals, glasses, etc.) have been extensively developed with surface shading models (e.g., microfacet models [Cook and Torrance 1982; Walter et al. 2007]). Unfortunately, these widely-used shading models have limited capability to represent *wet porous materials*. Examples of this kind of materials include a damp road or wet sand (see Fig. 7). Generally, the porous materials are made of many tiny grains. After being filled with liquids, the materials become wet and appear darker. These appearances have become crucial for many applications, like wet roads in the autonomous driving simulation. However, it's challenging to simulate these materials, as it involves complex optical phenomena.

In the literature, wet porous materials can be represented at different levels-geometry, medium or surface materials. While modeling individual particle as a sphere [Peltoniemi and Lumme 1992] or an prolate spheroid [Kimmel and Baranoski 2007] is accurate, it leads to extensive memory and time cost. Another group of methods render wet or porous materials with radiative transfer equation (RTE) or its variant. However, they model saturation or porosity

of medium in an ad-hoc way, by tweaking the Henyey-Greenstein (HG) phase function parameters [Jensen et al. 1999] or unnormalized porosity-aware transmittance functions [Hapke 2008]. Either way leads to unrealistic rendering. To our knowledge, no foundational medium formulation considering both porosity and saturation exist. The final category of methods represents porous materials using a bidirectional reflectance distribution function (BRDF) [Hnat et al. 2006; Lu et al. 2006; Merillou et al. 2000], incorporating cylinder-shaped holes on the surface. While these approaches are practical, they struggle to accurately reproduce real-world effects and cannot simulate transmission phenomena.

In this paper, we aim to model a wet porous appearance with controllable physical parameters that closely replicate real-world effects while maintaining practicality. To this end, we propose a generalized anisotropic radiative transfer equation to model a wet porous medium considering both the porosity and saturation effect. At the core of our wet porous medium is a transmittable micro-ellipsoid model, analogous to the micro-flake model [Jakob et al. 2010], except with different particle shapes. In our model, each particle is represented with an ellipsoid, and the distribution of aggregated particles follows an ellipsoidal distribution. We derive phase function and anisotropic attenuation functions for both isolated and aggregated medium particles. While the generalized anisotropic RTE, along with the transmittable micro-ellipsoid model, allows rendering a wet porous medium, it requires a long convergence time. To address this issue, we further propose a practical surface appearance model within the position-free framework [Guo et al. 2018; Wang et al. 2022]—*WetSpongeCake*. Consequently, our *WetSpongeCake* model can faithfully reproduce wet porous materials with physical parameters (porosity and saturation). It can represent a wide range of appearances, including a piece of wet paper, saturated sand, or cloth. To summarize, our contributions include:

- a generalized anisotropic radiative transfer equation for wet porous medium, which can capture the effect of surrounding liquid on light propagation through particles,
- a micro-ellipsoid model for wet medium particles, which defines its phase function and attenuation functions, and
- a practical surface appearance model *WetSpongeCake* to represent wet porous materials with physical parameters.

2 RELATED WORK

2.1 Wet material models

Several groups of approaches have been proposed in the literature for representing wet materials, explicit simulations on randomly generated particles, medium-based models and surface-based BRDFs.

Methods in the first category represent individual particle as a sphere [Peltoniemi and Lumme 1992] or a prolate spheroid [Kimmel and Baranoski 2007], and then perform Monte Carlo simulations on randomly generated particles. These methods are computationally expensive and designed for specific material (e.g., sand).

In the second category, Jensen et al. [1999] capture the saturation of materials using a combined surface and subsurface model, leveraging a two-term Henyey-Greenstein (HG) phase function to approximate the scattering of particles. While their method produces convincing results, it lacks physically meaningful parameters,

requiring manual adjustments of the HG parameter for control. Meanwhile, other studies [Hapke 1999, 2008; Shkuratov et al. 1999] introduce a porosity parameter by modifying the original RTE. However, these medium-based approaches rely on volumetric path tracing, which results in significant computational costs. Additionally, several other methods [Meng et al. 2015; Moon et al. 2007; Müller et al. 2016] have been proposed for simulating light transport in visible discrete particles, but these fall outside the scope of our work.

In the third category, several studies represent wet materials using surface-based models, including Lekner and Dorf [1988] and Bajo et al. [2021]. The former is based on Angstrom’s model [1925], while the latter improves upon Lekner et al.’s model [1988]. Other real-time surface models [Hnat et al. 2006; Lu et al. 2006; Merillou et al. 2000] introduce a cylindrical shape for holes and apply intrinsic roughness to the hole surfaces. These approaches are lightweight and practical. However, they struggle to closely match real-world effects. As pointed out by Twomey et al. [1986], even a minor refractive index (IOR) difference (e.g., water vs. benzene on wet sand [Bohren 1983]) can cause significantly different appearances, which surface models cannot accurately capture. More recently, d’Eon proposed several shading models [d’Eon 2021; d’Eon and Weidlich 2024] to describe porous, diffuse-like BRDFs. While these models provide analytic solutions for porous materials, they do not account for the saturation effect. Lucas et al. [2023; 2024] model porous layers, such as dust or dirt, where grains are distributed on a surface. In contrast, our work models porous materials, such as sand or walls, where particles are distributed throughout the volume.

2.2 Position-free BSDFs

The position-free property was first introduced in volumetric BSDF models by Dupuy et al. [2016], which start the trend of volumetric BSDF models. Guo et al. [2018] reformulate path integral within a medium from the entire spatial dimensions to the depth dimension only, as the incident and exit rays share the same position. This simplification of the path integral leads to a more efficient BSDF evaluation. This idea has been used further by Xia et al. [2020] and Gamboa et al. [2020] for more advanced sampling approaches or modeling pearlescent pigments [Guillén et al. 2020]. Wang et al. [2022] further generalize single-scattering to handle finite-thickness slabs with transmission. Their *SpongeCake* model simplified the computation by treating materials as volume slabs without surface interfaces. They also approximated multiple scattering using single scattering with adjusted parameters, making BSDF evaluations efficient and noise-free. Our surface appearance model also follows the position-free framework as a practical solution for wet porous medium rendering.

2.3 Micro-flake model

The micro-flake model, introduced by Jakob et al. [2010], was created to capture the complex anisotropic behavior of participating media by modeling the distribution of reflective micro-flakes. Later, Heitz et al. [2015] introduced the symmetric GGX (SGGX) representation, which uses 3×3 positive-definite matrices to efficiently describe micro-flake distributions. This method is flexible, allowing for both surface-like and fiber-like micro-flakes, with easy control over their

Table 1. Notations.

Mathematical notation	
Ω	full spherical domain
$\cos \omega$	The cosine of the angle between ω and the z-axis
$\omega_i \cdot \omega_o$	dot product
Physical quantities	
ω_i	incident direction
ω_o	outgoing direction
$f_p(\theta)$	phase function
Phase function parameters	
η_p	refractive index of particle
σ_p	particle projected area
Medium parameters	
σ	normal projected area
Z	thickness
S	saturation
P	porosity
α	single-scattering albedo
η_l	refractive index of liquid
σ_t^l	liquid extinction coefficient

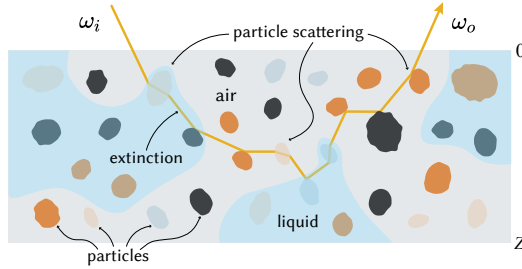


Fig. 2. Wet porous material is made of discrete particles, air, and liquid. After a light ray enters this material, it can be either reflected or refracted by the particle surface and travels in the air or the liquid. The ray is bounced within this material until it leaves the surface.

orientation. However, the micro-flake model treats each particle as an ideal disk, which limits its ability to represent transmittable particles.

3 WET POROUS MATERIALS WITH VOLUME RENDERING

In this section, we first introduce the underlying optical effects of wet porous materials (Sec. 3.1). Next, we modify the radiative transfer equation to account for porosity and saturation (Sec. 3.2).

3.1 Wet porous materials

Wet porous materials are composed of millions of non-spherical particles distributed in air and liquid, forming a complex volume, as illustrated in Fig. 2. The particles allow both reflection and transmission. These particles are characterized by intrinsic properties such as refractive index η_p and albedo α , while their orientations follow a specific distribution. The porosity, P , represents the fraction of the volume not occupied by particles. The liquid within the material has

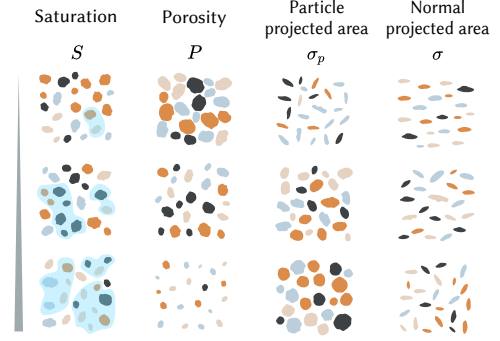


Fig. 3. Several examples of parameters defined on particles and medium.

a refractive index η_l and an extinction coefficient σ_t^l . The fraction of the liquid occupying the non-particle volume is defined as the saturation S . All parameters are summarized in Table 1.

When a light ray enters the medium, it interacts with particle surfaces, where it is either reflected or refracted. Between interactions, the ray travels through air or liquid, with the liquid absorbing some of its energy. The ray continues to bounce within the material until it exits the volume. Due to the finite thickness (Z) of the volume, the ray can either be reflected (exiting on the same side as its entry) or transmitted (exiting on the opposite side). The refraction between air and liquid occurring within the medium is ignored, following previous work [Kimmel and Baranoski 2007]. We do not consider diffraction effects, as the diffraction patterns in a densely packed particulate media are altered by the proximity of neighboring particles, making diffraction effects negligible, as discussed by Hapke [2008].

3.2 Generalized RTE considering porosity and saturation

The anisotropic RTE [Jakob et al. 2010] is formulated as:

$$(\omega \cdot \nabla)L(\omega) = -\sigma_t(\omega)L(\omega) + \sigma_s(\omega) \int_{\Omega} f_p(\omega' \cdot \omega)L(\omega')d\omega' + Q(\omega), \quad (1)$$

where σ_t and σ_s are the extinction and scattering coefficients respectively. Q is the source term. Note that the dependence on the position in Eqn. (1) is ignored for compactness.

The anisotropic radiative transfer equation allows for anisotropic scattering in the sense that the scattered intensity depends on the scattering angle. However, it does not take into account porosity and saturation, which limits its ability to represent wet porous materials. To enhance its representation capabilities, we incorporate both porosity and saturation into the anisotropic RTE.

Porosity. Porosity describes the fraction of the medium that is not occupied by particles. Hapke [2008] incorporated porosity into the RTE by treating the discrete medium as a series of discrete layers of particles, resulting in a discontinuous stair-step transmittance. Then, the discontinuous transmittance is transformed into an equivalent continuous function as an approximation:

$$T(t) = Ke^{-K\sigma_t t}, \quad (2)$$

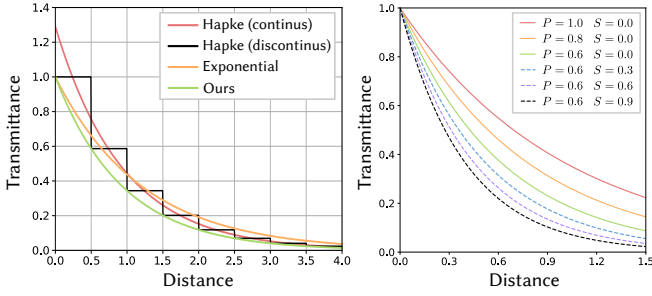


Fig. 4. Left: Comparison of several transmittance functions w.r.t. the traveling distance. Our saturation is set as 0. Right: our transmittance function as a function of the distance across several parameters.

where K is a key factor related to the porosity, derived by considering the that adjusts both the initial value and the extinction rate of the transmittance. When the particles are large compared to the wavelength, K is only affected by the porosity P , hence:

$$K = -\frac{\ln\left(1 - \left(\frac{3\sqrt{\pi}}{4}(1-P)\right)^{\frac{2}{3}}\right)}{\left(\frac{3\sqrt{\pi}}{4}(1-P)\right)^{\frac{2}{3}}}, \quad (3)$$

the detailed derivation is shown in the supplementary.

While Eqn. (3) models porosity, it can not ensure energy conservation, as the transmittance can exceed 1. Inspired by Hapke's work, we modify the anisotropic RTE [Jakob et al. 2010] to incorporate porosity in a simple yet energy-conserving manner by introducing the porosity-related factor K into the coefficients:

$$(\omega \cdot \nabla)L(\omega) = -K\sigma_t(\omega)L(\omega) + K\sigma_s(\omega) \int_{\Omega} f_p(\omega' \cdot \omega) L(\omega') d\omega' + Q(\omega), \quad (4)$$

where K behaves like the density; as porosity decreases, K increases, leading to a denser medium. In our formulation, the transmittance function starts at 1, ensuring energy conservation.

We compare Hapke's discontinuous stair-step transmittance, its continuous approximation, traditional exponential transmittance, and our transmittance in Fig. 4. Clearly, Hapke's continuous approximation starts with an initial value greater than 1, which violates the principle of energy conservation. In contrast, our transmittance, $T(t) = e^{-(K\sigma_t)t}$, not only ensures energy conservation but also also takes porosity effects into account.

Saturation. After porous materials are wetted by a liquid, the fraction of the liquid occupying the non-particle volume is defined as saturation S . This saturation also influences the anisotropic RTE. We assume that the liquid is an absorption-only medium. When the liquid permeates the medium, the distribution of particles remains unchanged, as the liquid simply replaces the air fraction. Under these assumptions, light extinction in the medium is influenced by both the particles and the liquid. While the attenuation caused by the particles has been modeled in Eqn. (4), the additional attenuation resulting from the liquid must be considered as well. Therefore, the anisotropic RTE considering porosity and saturation can be

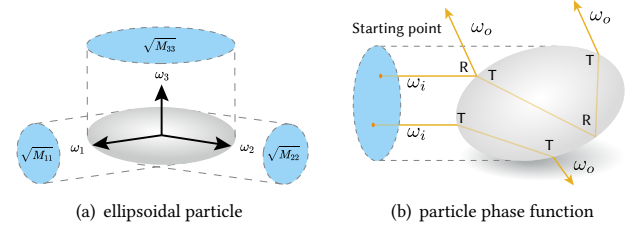


Fig. 5. (a) Each particle is modeled as an ellipsoid, defined by eigenvectors (ω_1, ω_2 and ω_3) and eigenvalues, where ω_3 is aligned with the ellipsoid normal. (b) the particle phase function is defined as the possibility of all paths originating from the projected area of ω_i , traveling in direction ω_i , bouncing within the ellipsoid, and finally exiting in direction ω_o .

formulated:

$$(\omega \cdot \nabla)L(\omega) = - (K\sigma_t(\omega) + S\sigma_t^l)L(\omega) + K\sigma_s(\omega) \int_{\Omega} f_p(\omega' \cdot \omega) L(\omega') d\omega' + Q(\omega), \quad (5)$$

where σ_t^l is the liquid's extinction coefficient. The transmittance is obtained by integrating extinction of light along ω , yielding:

$$T(t) = e^{-(K\sigma_t + S\sigma_t^l)t}. \quad (6)$$

Note that when $P = 1$ and $S = 0$, the above transmittance reduces to the typical exponential transmittance. In Fig. 4 (right), we illustrate the transmittance as a function of distance for various materials with different porosity and saturation.

4 TRANSMITTABLE MICRO-ELLIPSOID MODEL

To render a wet porous medium with the generalized anisotropic RTE (Sec. 3.2), we must establish the characteristics of the particles within the medium. Existing isotropic or anisotropic medium models have focused mainly on particles (micro-flake) that can reflect light and have not addressed transmittable particles. However, transmittability is essential for accurately representing a wet porous medium. In our model, we represent each particle as an ellipsoid, which allows for the modeling of an anisotropic medium while also enabling the transmittability of light. We will first define several key functions for isolated particles (Sec. 4.1) and then present the statistical functions for aggregated particles (Sec. 4.2).

4.1 Isolated ellipsoidal particle

Similar to the non-spherical particle by Jakob et al. [2010], we need to define several functions to characterize a particle: 1) projected area $\sigma(\omega)$ is the area of the particle's projection onto ω^\perp ; 2) particle phase function $p(\omega_i, \omega_o)$ represents the probability of the light scattering into ω_o , illuminated from direction ω_i .

Projected area. Each particle is represented as an ellipsoid with normal m , as shown in Fig. 5. By setting orthonormal eigenvectors ($\omega_1, \omega_2, \omega_3$), where $\omega_3 = m$, together with the projected area σ_p onto ω_1 and ω_2 , an ellipsoid can be established. It can be represented as a 3×3 symmetric positive definite matrix M_p :

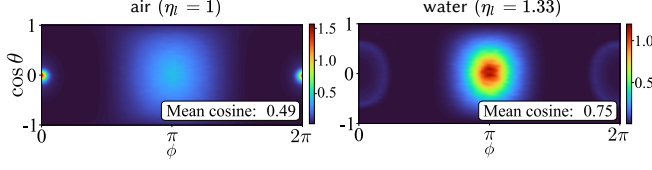


Fig. 6. Visualization of the phase function for particles surrounded by air and water, respectively, with the mean cosine value provided in the bottom-right corner. The remaining parameters are set to $\eta_p = 1.8$, $\sigma = 1$, and $\sigma_p = 1$. Additional results are provided in the supplementary material.

$$M_p = (\omega_1, \omega_2, \omega_3) \begin{pmatrix} M_{11} & 0 & 0 \\ 0 & M_{22} & 0 \\ 0 & 0 & M_{33} \end{pmatrix} (\omega_1, \omega_2, \omega_3)^T, \quad (7)$$

where $M_{11} = \sigma^2(\omega_1) = \sigma_p^2$, $M_{22} = \sigma^2(\omega_2) = \sigma_p^2$ and $M_{33} = \sigma^2(\omega_3) = 1$ are positive eigenvalues of M . The projected area of an ellipsoid with normal m onto direction ω can be computed as:

$$\sigma(m, \omega) = \sqrt{\omega^T M_p \omega}. \quad (8)$$

Particle phase function. In contrast to the micro-flake model, which defines the particle phase function on a flat disk with a constant flake normal, our particle phase function is defined on an ellipsoid. Here, our particle phase function $p(\omega_i, \omega_o)$ represents the probability of all light paths exiting in direction ω_o , given an entry direction ω_i with all possible entry points located on the ellipsoid surface. For a given entry point x_i , the light might have various types of light paths, denoted by R, TT, TRT, \dots , where R stands for reflection and T stands for transmission, resulting in a probability:

$$p_i(x_i) = \sum_{t \in \mathcal{T}} A_t \quad (9)$$

Here, A_t indicates the attenuation stemming from the Fresnel term along a specular path of type $t \in \mathcal{T}$, where \mathcal{T} represents the set of all possible combinations of R and T .

Then, we need to consider all the possible entry points x_i on the ellipsoid surface. To do this, we equivalently transform it into all light paths starting from the projected area of ω_i . This way, the particle phase function can be formulated as

$$p(\omega_i, \omega_o) = \int_{\sigma(\omega_i)} p_i(x_i) dA x_i, \quad (10)$$

where $dA x_i$ is the differential area around x_i .

Deriving a closed-form expression for the particle phase function is quite challenging. To address this, we estimate Eqn. (10) with Monte Carlo simulation by sampling the projected area of ω_i , shooting a ray at that direction, intersecting the ray with the ellipsoid to determine an entry point x_i . From x_i , the following specular paths are also sampled by choosing reflection or refraction at each interaction. When the ray exits the ellipsoid, we record its exit direction. This way, we tabulate the particle phase function as a 3D lookup table. Note that the one-dimension reduction is due to the azimuthal symmetry of the particle shape about the normal. For more detailed information, please refer to supplementary material.

4.2 Micro-ellipsoid model

Built on the isolated particle, we propose our micro-ellipsoid model, which is statistically defined for aggregated ellipsoidal particles. We assume the normal distribution of these aggregated ellipsoidal particles follows an ellipsoidal distribution, similar to the SGGX model [Heitz et al. 2015]:

$$D(\omega_m) = \frac{1}{\pi \sqrt{|M_n|} (\omega_m^T M_n^{-1} \omega_m)^2}, \quad (11)$$

where M_n is the symmetric positive definite matrix to describe the normal distribution, and ω_m is the micro-ellipsoid normal.

Attenuation coefficients. Next, we present another key function: the attenuation coefficients $\sigma_t(\omega)$ and $\sigma_s(\omega)$. Jakob et al. [2010] provided a general formulation for these functions:

$$\begin{aligned} \sigma_t(\omega) &= \int_{\Omega} \sigma(\omega_m, \omega) D(\omega_m) d\omega_m, \\ \sigma_s(\omega) &= \alpha \sigma_t(\omega). \end{aligned} \quad (12)$$

By applying the particle projected area function Eqn. (8), we have formulation of our attenuation coefficients.

Phase function. It is essential to consider the medium's saturation, as it influences the IOR, which is a key factor in the phase function. With liquid in the medium, there are two cases of particle interface: air-particle and liquid-particle. We define the phase function for these two cases (p_d and p_w), and then interpolate them w.r.t. the saturation:

$$\begin{aligned} f_p(\omega_i, \omega_o) &= \frac{1-S}{\sigma_t(\omega_i)} \int_{\Omega} p_d(\omega_m, \omega_i, \omega_o) \sigma(\omega_m, \omega_i) D(\omega_m) d\omega_m + \\ &\quad \frac{S}{\sigma_t(\omega_i)} \int_{\Omega} p_w(\omega_m, \omega_i, \omega_o) \sigma(\omega_m, \omega_i) D(\omega_m) d\omega_m. \end{aligned} \quad (13)$$

We now have the formulations for both the attenuation coefficients and the phase function, although neither has analytical solutions. Therefore, in practice, we compute these functions using Monte Carlo estimation and store the results in a 3D lookup table for the phase function and a 1D lookup table for the attenuation coefficients, as explained in supplementary material.

In Fig. 6, we visualize two phase functions with different liquid IORs but the same particle IOR. The results show that surrounding the particle with liquid leads to increased forward scattering compared to when it is surrounded by air.

Properties and relationship to the micro-flake model. Our attenuation coefficients and phase function follows the framework by Jakob et al. [2010], ensuring both the system reciprocity and the normalization of the phase function.

Our micro-ellipsoid model and the micro-flake modelis have different particle shape, where our particle is an ellipsoid, and the micro-flake relies on a flake without any volume. The advantage of the ellipsoid is that it allows for transmittability, although it lacks a closed-form formulation. The micro-flake model can also be considered as a special case of our model, by setting $\sigma_p = 0$, which makes the ellipsoid into a disk.

4.3 Isotropic medium

In a special case, the particle shape become a sphere, by setting $\sigma_p = 1$, leading to an isotropic medium. In this scenario, the volume extinction coefficients σ_t and σ_s become constants:

$$\sigma_t = \int_{\Omega} D(\omega_m) d\omega_m, \quad \sigma_s = \alpha \sigma_t. \quad (14)$$

The particle phase function and the micro-ellipsoid phase function are also simplified and only depends on $\cos \theta = \omega_i \cdot \omega_o$:

$$f_p(\omega_i, \omega_o) = p(\omega_i, \omega_o) \frac{\int_{\Omega} \sigma(\omega_m, \omega_i) D(\omega_m) d\omega_m}{\sigma_t(\omega_i)} = p(\omega_i, \omega_o). \quad (15)$$

As the phase function only has one dimension, it can be easily represented by fitting a basis function. In practice, we use two Gaussians to represent the one-dimensional phase function: one for forward scattering and the other for backward scattering:

$$f_p(\theta, S) = w_1 \cdot G_1(\theta; \mu_1, \sigma_1) + w_2 \cdot G_2(\theta; \mu_2, \sigma_2), \quad (16)$$

$$G(x; \mu, \sigma) = \frac{1}{\sqrt{2\pi}\sigma} e^{-\frac{(x-\mu)^2}{2\sigma^2}},$$

where G_1 and G_2 are two one-dimensional Gaussian functions with μ_1 and μ_2 as the mean values, σ_1 and σ_2 as the variances. w_1 and w_2 are the weights for two Gaussians. All these parameters are obtained by optimization using the Monte Carlo simulation as GT.

5 WETSPONGECAKE: A BSDF MODEL WITH POROSITY AND SATURATION

We have already defined the medium, which still requires large sampling rates for convergence. To address this, we integrate it into the SpongeCake framework by treating the medium as a layer. We derive an analytical model for single scattering, taking into account both reflection and transmission. Then, we further introduce multiple scattering, delta transmission, and the air-liquid interface.

5.1 Single scattering

The single scattering within a medium with thickness Z can be computed by the integral over the depth of the single scattering vertex [Wang et al. 2022]. At each single scattering vertex, we compute phase function, the extinction of the particles and the liquid, together with cosine terms due to the change of the integration domain. Then, the BRDF and BTDF can be formulated as:

$$f_r(\omega_i, \omega_o) = \int_0^Z \frac{\alpha \sigma_t(\omega_i) f_p(\omega_i, \omega_o)}{\cos \omega_i \cos \omega_o} T\left(\frac{t}{\cos \omega_i}\right) T\left(\frac{t}{\cos \omega_o}\right) dt$$

$$= K \sigma_s(\omega_i) f_p(\omega_i, \omega_o) \frac{1 - e^{-\left(\sigma_i \frac{Z}{\cos \omega_i} + \sigma_o \frac{Z}{\cos \omega_o}\right)}}{\sigma_i \cos \omega_o + \sigma_o \cos \omega_i},$$

$$f_t(\omega_i, \omega_o) = \int_0^Z \frac{\alpha \sigma_t(\omega_i) f_p(\omega_i, \omega_o)}{|\cos \omega_i| |\cos \omega_o|} T\left(\frac{t}{|\cos \omega_i|}\right) T\left(\frac{Z-t}{|\cos \omega_o|}\right) dt$$

$$= K \sigma_s(\omega_i) f_p(\omega_i, \omega_o) \frac{e^{-\frac{\sigma_i Z}{|\cos \omega_i|}} - e^{-\frac{\sigma_o Z}{|\cos \omega_o|}}}{\sigma_o |\cos \omega_i| - \sigma_i |\cos \omega_o|}, \quad (17)$$

where $\sigma_i = K \sigma_t(\omega_i) + S \sigma_t^l$ and $\sigma_o = K \sigma_t(\omega_o) + S \sigma_t^l$. The single scattering can be computed using the precomputed phase function.

5.2 Multiple scattering

To compute multiple scattering efficiently, Wang et al. [2022] estimate the multiple scattering of a BSDF by mapping it into a single-scattering lobe with modified parameters along with a Lambertian term with a simple neural network. Their approach could be applied to our BSDF as well. However, the key challenge is that our phase function is not analytical but represented by a precomputed table, which lacks differentiability. To address this limitation, we represent phase function using a neural network to enable multiple to single scattering mapping.

Specifically, we propose a phase function network and a parameter mapping network. The former transforms phase function parameters into a phase function value using a simple multi-layer perceptron (MLP). The parameter mapping network converts multiple scattering parameters into single scattering parameters, together with a Lambertian parameter and their weights. The phase function neural network is trained first. Afterward, the mapping network is trained by rendering the predicted single scattering parameters with the learned phase function network. Once the mapping network is trained, we tabulate the phase function to avoid network inference during rendering. More details are in the supplementary.

Please note that we do not utilize the neural representation of the phase function for the single scattering, as it is much sharper, which is beyond the capabilities of the learned network.

In the case of an isotropic medium, since the phase function can be represented using two Gaussian distributions, we can directly learn the mapping network without the need to train an additional phase function neural network.

5.3 The other components

Delta transmission. For a thin medium, light can pass through without any scattering, such as paper and cloth. This delta function can be determined by analyzing the transmission of light through the medium in the direction of ω_i , similar to the SpongeCake model.

Air-liquid interface. When a material is fully saturated ($S = 1$), a thin film of liquid forms on the surface. Our model captures the effects of light reflection and refraction at the interface by layering a dielectric BSDF on top of the medium.

Importance sampling. Importance sampling is a necessary component for a BSDF. For this, we use a simple solution, by sampling the phase function with cumulative distribution function to get the outgoing direction.

6 RESULTS

We have implemented our algorithm inside the Mitsuba renderer [2010]. All timings in this section are measured on a 2.20GHz Intel i7 (48 cores) with 32 GB of main memory. We provide the material settings in the supplementary material.

6.1 Model validation

We validate our model through a series of experiments, including comparisons against photographs, equal-time comparison between the surface model and volume model, validation of multiple scattering, and the white furnace test. Please note that our multiple

scattering model is applied to all materials, except for the spatially varying anisotropic material, for which we perform a random walk in a position-free framework [Guo et al. 2018].

Sand scene. To demonstrate WetSpongeCake’s capability to replicate natural appearances, we compare our model, Jensen et al. [1999], which employs two Henyey-Greenstein (HG) lobes as the phase function, along with a real photograph. The comparison is shown in Fig. 7. This scene consists of three types of sand (isotropic) in different containers: dry, saturated with water, and saturated with ink, respectively, lit under an environment map and a directional light. We render this scene with both single and multiple scattering, considering global illumination. Our model almost matches the photograph, while Jensen et al.’s method, which adjusts HG parameters manually, can not model liquid absorption.

Cloth scene. In Fig. 8, we compare our method, the albedo map method, which achieves darker reflections by adjusting the albedo, along with a real photograph. The scene consists of a wet cloth (anisotropic medium) under two lighting conditions: front-lit and back-lit. We render this scene with both single and multiple scattering. The photographs demonstrate that the wet regions of the cloth exhibit reduced reflection and enhanced transmission, a behavior accurately captured by our model. In contrast, simply modifying the albedo reduces both reflection and transmission, failing to reproduce the desired appearance.

Our volume model vs. our surface model. We validate the effectiveness of our surface model (both single and multiple scattering), by comparing it to our volume model in Fig. 12, where the converged volume renderings are treated as GT. We find that the result of our single scattering is almost identical to the GT while having much less noise than the volume rendering with equal time, as it is analytical and does not need a random walk. After introducing the multiple scattering, the result of our surface model still exhibits less noise and lower error than volume rendering with equal time, thanks to our effective way of computing the multiple scattering.

Multiple scattering validation. In Figs. 13 and 14, we validate our multiple scattering by comparing its results to the GT obtained by Monte Carlo random walk [Guo et al. 2018] across various materials. The results demonstrate an overall good match, except in cases with a low projected area where the sharp distribution cannot be accurately expressed by the phase function network.

White furnace test. We perform a white furnace test for our surface model on materials with no absorption, under a constant environment map with radiance set as one. As shown in Fig. 11, the delta transmission and the single scattering results in darker pixel values, as expected. When including the multiple scattering using Monte Carlo random walk, a constant image was produced, while our multiple scattering closely approximates a constant image, although there are some inaccuracies due to network bias.

Sculpture Scene. To demonstrate the impact of different parameters on appearance, we present renderings of the Sculpture scene under various parameter settings in Fig. 15. This scene is illuminated by two area light sources and an environment map. As the liquid’s IOR increases, the phase function becomes more forward-scattering,

causing a darker appearance. Similarly, higher saturation enhances forward scattering while incorporating liquid absorption, further darkening the sculpture. Furthermore, increased light absorption by the liquid results in a noticeably darker sculpture.

6.2 More results

Teaser scene. In Fig. 1, we show several objects with porous materials lit by an environment map with global illumination, including wet cloths (anisotropic), flowerpots (isotropic), and sculptures (isotropic). Our BSDF can represent a wide range of appearances in the real world with high fidelity, controlled by physical parameters.

Paper scene. We design a Paper scene using the photo converted to a grayscale image as a saturation map, as shown in Fig. 10. The saturation map, displayed in the bottom-right corner of the rendered image, defines the varying saturation across the surface. This scene is illuminated by an environment map, taking global illumination into account. Our model is able to produce the desired effects.

Table scene. In Fig. 9, we present the appearance effects caused by the air-liquid interface. This scene consists of wood (isotropic), illuminated by an environment map, with global illumination taken into account. The table surface without a liquid film appears diffuse, while the table surface with a liquid film exhibits a specular lobe.

6.3 Discussion and limitations

We have identified several limitations in our method. Our model does not have closed-form formulations and relies on precomputation, which restricts its ability to represent multiple scattering in spatially varying anisotropic materials. Additionally, similar to previous studies [Wang et al. 2022], our multiple scattering network may sometimes struggle to achieve accurate fits.

7 CONCLUSION

In this paper, we have presented a transmittable micro-ellipsoid model for rendering wet porous materials, applicable for both volume and surface appearance rendering. We generalize the anisotropic radiative transfer equation to account for both porosity and saturation, which enables volume rendering of wet porous materials together with the micro-ellipsoid model. Building on this foundation, we then derive a practical surface appearance model under the position-free framework, termed WetSpongeCake. The WetSpongeCake model effectively represents the diverse appearances of wet porous materials using physically meaningful parameters such as porosity and saturation, and it captures both reflection and transmission effects. The resulting appearances closely mimic real-world observations. To the best of our knowledge, no existing method offers such a lightweight, physically-based shading model for wet porous materials. Finding a closed-form solution for the phase function is crucial for completing the theory and further enhancing the model’s practical applicability. We also believe that our model has potential applications in other areas, such as inverse rendering.

REFERENCES

- Juan Miguel Bajo, Claudio Delrieux, and Gustavo Patow. 2021. Physically inspired technique for modeling wet absorbent materials. *The Visual Computer* 37, 8 (2021), 2053–2068.
- Craig Bohren. 1983. Simple Experiments in Atmospheric Physics: Multiple Scattering at the Beach. *Weatherwise* 36, 4 (1983), 197–200. <https://doi.org/10.1080/00431672.1983.9930144> arXiv:<https://doi.org/10.1080/00431672.1983.9930144>
- Robert L. Cook and Kenneth E. Torrance. 1982. A Reflectance Model for Computer Graphics. *ACM Trans. Graph.* 1, 1 (Jan. 1982), 7–24.
- Eugene d'Eon. 2021. An analytic BRDF for materials with spherical Lambertian scatterers. In *Computer Graphics Forum*, Vol. 40. Wiley Online Library, 153–161.
- Eugene d'Eon and Andrea Weidlich. 2024. VMF Diffuse: A Unified Rough Diffuse BRDF. *Computer Graphics Forum* (2024). <https://doi.org/10.1111/cgf.15149>
- Jonathan Dupuy, Eric Heitz, and Eugene d'Eon. 2016. Additional Progress Towards the Unification of Microfacet and Microflake Theories. In *EGSR - Experimental Ideas & Implementations*. The Eurographics Association, 55–63.
- Luis E. Gamboa, Adrien Gruson, and Derek Nowrouzezahrai. 2020. An Efficient Transport Estimator for Complex Layered Materials. *Computer Graphics Forum* 39, 2 (2020), 363–371.
- Ibón Guillén, Julio Marco, Diego Gutierrez, Wenzel Jakob, and Adrien Jarabo. 2020. A General Framework for Pearlescent Materials. *Transactions on Graphics (Proceedings of SIGGRAPH Asia)* 39, 6 (Nov. 2020). <https://doi.org/10.1145/3414685.3417782>
- Yu Guo, Miloš Hašan, and Shuang Zhao. 2018. Position-Free Monte Carlo Simulation for Arbitrary Layered BSDFs. *ACM Trans. Graph.* 37, 6, Article 279 (Dec. 2018), 14 pages.
- Bruce Hapke. 1999. Scattering and Diffraction of Light by Particles in Planetary Regoliths. *Journal of Quantitative Spectroscopy and Radiative Transfer* 61, 5 (1999), 565–581. [https://doi.org/10.1016/S0022-4073\(98\)00042-9](https://doi.org/10.1016/S0022-4073(98)00042-9)
- Bruce Hapke. 2008. Bidirectional reflectance spectroscopy: 6. Effects of porosity. *Icarus* 195, 2 (2008), 918–926. <https://doi.org/10.1016/j.icarus.2008.01.003>
- Eric Heitz, Jonathan Dupuy, Cyril Crassin, and Carsten Dachsbacher. 2015. The SGGX Microflake Distribution. *ACM Trans. Graph.* 34, 4, Article 48 (July 2015), 11 pages.
- Kevin Hnat, Damien Porquet, Stéphane Merillou, and Djamchid Ghazanfarpour. 2006. Real-Time Wetting of Porous Media. *MG&V* 15, 3 (jan 2006), 401–413.
- Wenzel Jakob. 2010. Mitsuba renderer. <http://www.mitsuba-renderer.org>.
- Wenzel Jakob, Adam Arbree, Jonathan T. Moon, Kavita Bala, and Steve Marschner. 2010. A Radiative Transfer Framework for Rendering Materials with Anisotropic Structure. In *ACM SIGGRAPH 2010 Papers (SIGGRAPH '10)*. Article 53, 13 pages.
- Henrik Wann Jensen, Justin Legakis, and Julie Dorsey. 1999. Rendering of Wet Materials. In *Proceedings of the 10th Eurographics Conference on Rendering (EGWR'99)*. Eurographics Association, Goslar, DEU, 273–282.
- Bradley W. Kimmel and Vladimir V.G. Baranowski. 2007. A novel approach for simulating light interaction with particulate materials: application to the modeling of sand spectral properties. *Opt. Express* 15, 15 (Jul 2007), 9755–9777. <https://doi.org/10.1364/OE.15.009755>
- John Lekner and Michael C. Dorf. 1988. Why some things are darker when wet. *Appl. Opt.* 27, 7 (Apr 1988), 1278–1280. <https://doi.org/10.1364/AO.27.001278>
- Jianye Lu, Athinodoros S. Georgiades, Holly Rushmeier, Julie Dorsey, and Chen Xu. 2006. Synthesis of material drying history: phenomenon modeling, transferring and rendering. In *ACM SIGGRAPH 2006 Courses (SIGGRAPH '06)*. Association for Computing Machinery, New York, NY, USA, 6–es. <https://doi.org/10.1145/1185657.1185726>
- Simon Lucas, Mickael Ribardiere, Romain Pacanowski, and Pascal Barla. 2023. A Micrograin BSDF Model for the Rendering of Porous Layers. In *SIGGRAPH Asia 2023 Conference Papers (SA '23)*. Association for Computing Machinery, New York, NY, USA, Article 40, 10 pages. <https://doi.org/10.1145/3610548.3618241>
- Simon Lucas, Mickael Ribardiere, Romain Pacanowski, and Pascal Barla. 2024. A Fully-correlated Anisotropic Micrograin BSDF Model. *ACM Transactions on Graphics* 43, 4 (2024), 111.
- Johannes Meng, Marios Papas, Ralf Habel, Carsten Dachsbacher, Steve Marschner, Markus Gross, and Wojciech Jarosz. 2015. Multi-scale modeling and rendering of granular materials. *ACM Trans. Graph.* 34, 4, Article 49 (jul 2015), 13 pages. <https://doi.org/10.1145/2766949>
- S. Merillou, J.-M. Dischler, and D. Ghazanfarpour. 2000. A BRDF postprocess to integrate porosity on rendered surfaces. *IEEE Transactions on Visualization and Computer Graphics* 6, 4 (2000), 306–318. <https://doi.org/10.1109/2945.895876>
- Jonathan T. Moon, Bruce Walter, and Stephen R. Marschner. 2007. Rendering discrete random media using precomputed scattering solutions. In *Proceedings of the 18th Eurographics Conference on Rendering Techniques (EGSR '07)*. Eurographics Association, Goslar, DEU, 231–242.
- Thomas Müller, Marios Papas, Markus Gross, Wojciech Jarosz, and Jan Novák. 2016. Efficient rendering of heterogeneous polydisperse granular media. *ACM Trans. Graph.* 35, 6, Article 168 (dec 2016), 14 pages. <https://doi.org/10.1145/2980179.2982429>
- Jouni I. Peltoniemi and Kari Lumme. 1992. Light scattering by closely packed particulate media. *J. Opt. Soc. Am. A* 9, 8 (Aug 1992), 1320–1326. <https://doi.org/10.1364/JOSAA.9.001320>
- Yurij Shkuratov, Larissa Starukhina, Harald Hoffmann, and Gabriele Arnold. 1999. A Model of Spectral Albedo of Particulate Surfaces: Implications for Optical Properties of the Moon. *Icarus* 137, 2 (1999), 235–246. <https://doi.org/10.1006/icar.1998.6035>
- Sean A. Twomey, Craig F. Bohren, and John L. Mergenthaler. 1986. Reflectance and albedo differences between wet and dry surfaces. *Appl. Opt.* 25, 3 (Feb 1986), 431–437. <https://doi.org/10.1364/AO.25.000431>
- Bruce Walter, Stephen R. Marschner, Hongsong Li, and Kenneth E. Torrance. 2007. Microfacet Models for Refraction through Rough Surfaces. In *Rendering Techniques (proc. EGSR 2007)*. The Eurographics Association, 195–206.
- Beibei Wang, Wenhua Jin, Miloš Hašan, and Ling-Qi Yan. 2022. SpongeCake: A Layered Microflake Surface Appearance Model. *ACM Trans. Graph.* 42, 1, Article 8 (sep 2022), 16 pages. <https://doi.org/10.1145/3546940>
- Mengqi (Mandy) Xia, Bruce Walter, Christophe Hery, and Steve Marschner. 2020. Gaussian Product Sampling for Rendering Layered Materials. *Computer Graphics Forum* 39, 1 (2020), 420–435.
- Anders Ångström. 1925. The Albedo of Various Surfaces of Ground. *Geografiska Annaler* 7 (1925), 323–342. <http://www.jstor.org/stable/519495>

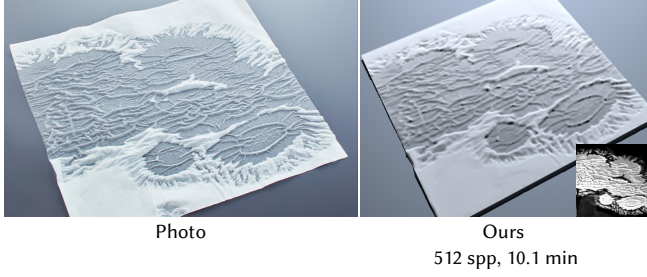


Fig. 10. A wet paper saturated by water. Our method is able to characterize the saturation level using a saturation map.

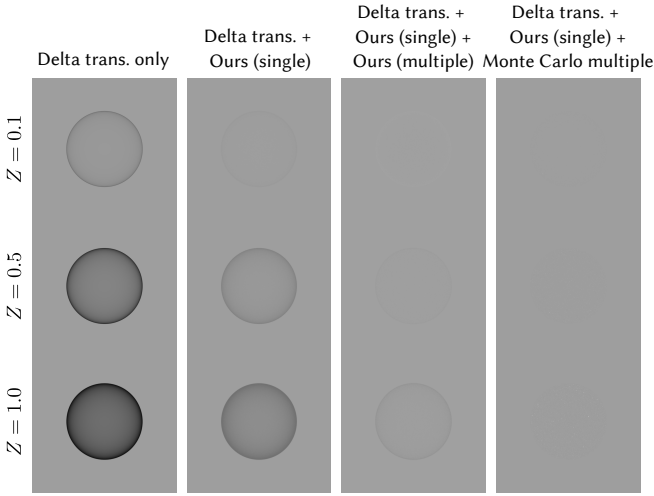


Fig. 11. A white furnace test for a WetSpongeCake material with no absorption. While the delta transmission and single scattering result in darker pixel values, our multiple scattering model produces an image that is nearly uniform, with minor inaccuracies. The Monte Carlo multiple scattering successfully passes the white furnace test.

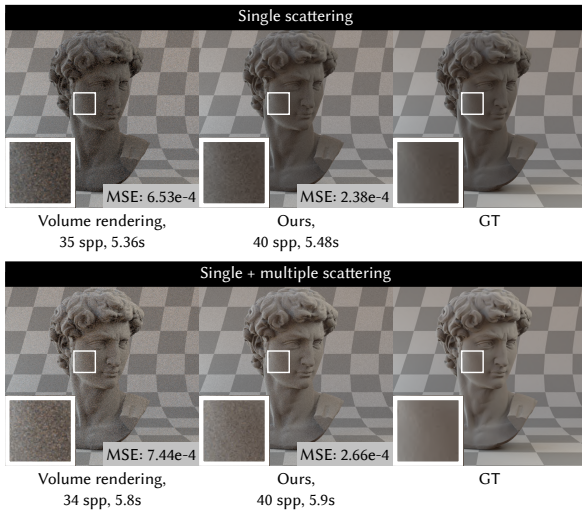


Fig. 12. Comparison between our BSDF surface model and the volume rendering with our modified RTE. The references are rendered with our modified RTE at a high sample rate. In both cases, our BSDF produces results with much less noise and lower error than the volume renderings with equal time.



Fig. 7. Comparison between the photograph, our model, and the two-HG method by Jensen et al. [1999]. Our model demonstrates a close match with the photograph, whereas the two-HG method by Jensen et al. [1999] captures the change in scattering direction but fails to adequately model liquid absorption.

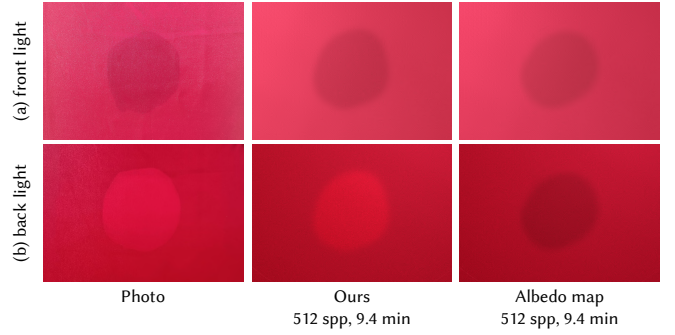


Fig. 8. Comparison between photographs, our model, and an empirical approach which modifies the albedo at two light conditions (front-lit and back-lit). In the photographs, the wet regions of the cloth exhibit reduced reflection and enhanced transmission. Our model replicates these effects accurately, whereas using a darker albedo achieves a similar reduction in reflection but results in incorrect darkening of transmission.

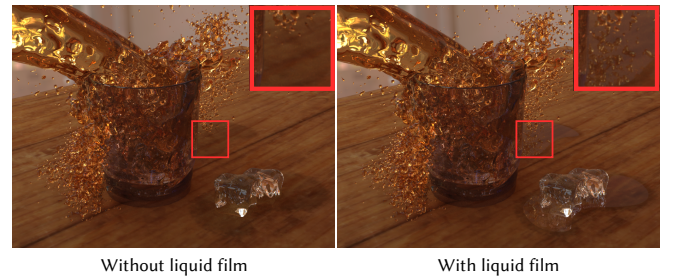


Fig. 9. Our model supports a thin liquid film on top of the medium, capturing the reflection induced by the air-liquid interface.

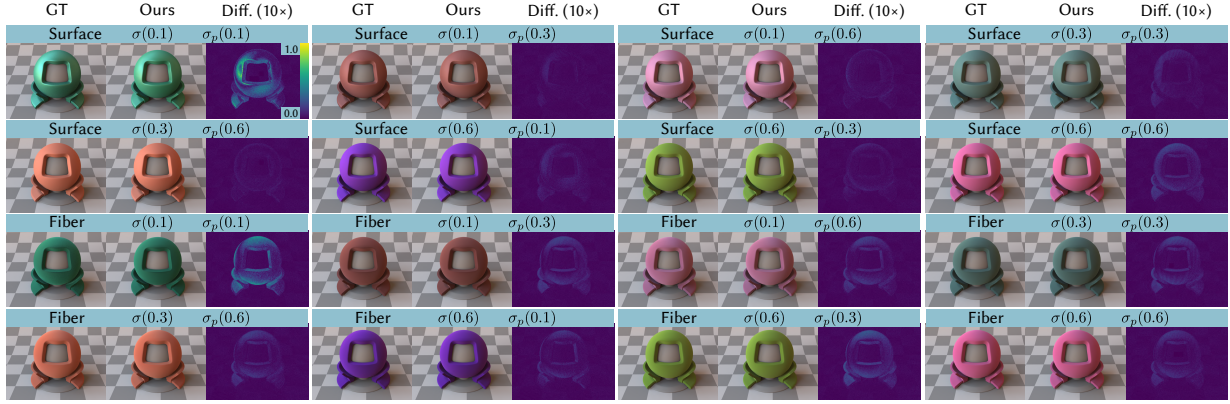


Fig. 13. Multiple scattering validation. For each example, we provide the normal projected area σ , particle projected area σ_p . The ground truth is obtained through Monte Carlo simulation of multiple scattering. Our results exhibit minor differences from the ground truth in most cases.

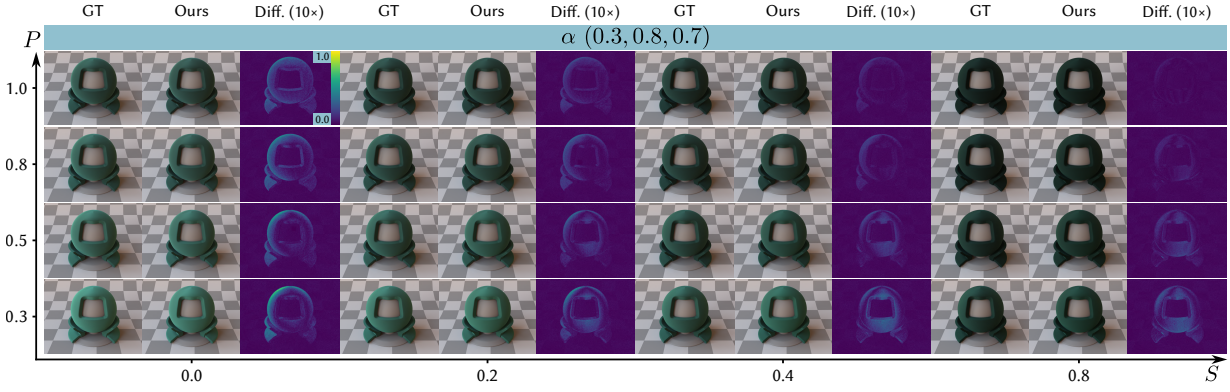


Fig. 14. Multiple scattering validation for a set of materials, with varying porosity P and saturation S . Monte Carlo simulation of multiple scattering is used as the ground truth. Our results show only minor deviations from the ground truth.

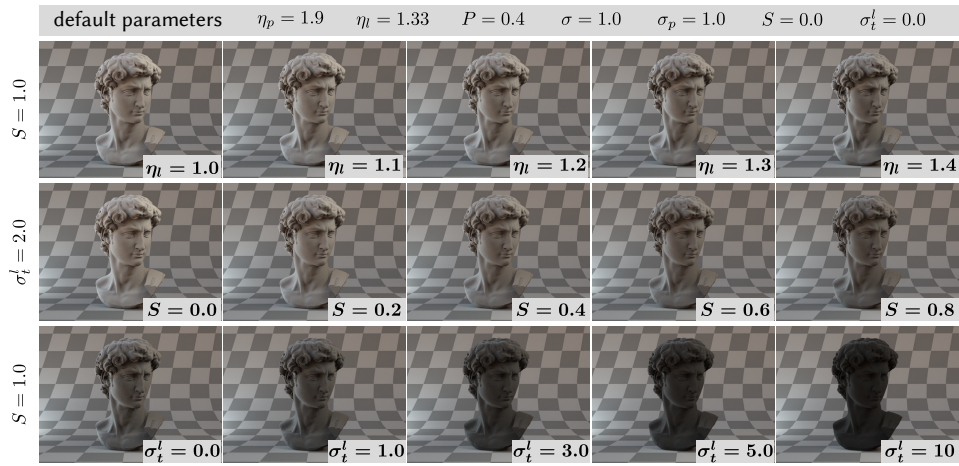


Fig. 15. Sculpture scene under different parameter settings. Parameters not explicitly mentioned are set to their default values, as indicated at the top of the figure.

Supplemental materials: A Micro-Ellipsoid Model for Wet Porous Materials Rendering

GAOLE PAN, Nanjing University of Science and Technology, China

YUANG CUI*, Anhui Science and Technology University, China

JIAN YANG, Nanjing University of Science and Technology, China

BEIBEI WANG†, Nanjing University, China

1 IMPLEMENTATION DETAILS

In this section, we present additional details about our implementation, including the simulation process for the particle phase function and the precomputation of the attenuation coefficients and phase function (Sec. 1.1). For WetSpongeCake, we provide further details on the neural network (Sec. 1.2).

1.1 Micro-ellipsoid model

particle phase function. The particle phase function is computed via Monte Carlo simulation and stored as a 3D lookup table. The center of the ellipsoid is positioned at the origin of the coordinate system, and the particle orientation ω_m aligns with the z-axis. For each incoming direction ω_i , we generate the starting point of the ray by sampling a disk located in the plane perpendicular to the incoming ray, ensuring that it can cover the entire ellipsoid. We then trace the ray and check for intersections with the ellipsoid. If no intersection occurs, the ray is discarded. If an intersection is found, we perform regular path tracing, where at each intersection, we decide whether the ray is reflected or refracted based on the Fresnel term as the probability. The process continues until the ray exits the particle.

We store the table with the following dimensions: the polar angle θ_i of ω_i , the polar angle θ_o of ω_o , and the azimuthal angle ϕ_o of ω_o . Due to the azimuthal symmetry of the particle shape about the normal m , the azimuthal angle of the incident direction can be omitted.

Attenuation coefficients and phase function. The attenuation coefficients and the phase function of the aggregated medium are computed using Monte Carlo estimation:

$$\sigma_t(\omega) = \frac{1}{N} \sum_{i=0}^{N-1} \frac{\sigma(\omega_m^i, \omega) D(\omega_m^i)}{\text{pdf}(\omega_m^i)}, \quad (1)$$

$$f_p(\omega_i, \omega_o) = \frac{1}{N} \sum_{i=0}^{N-1} \frac{p(\omega_m^i, \omega_i, \omega_o) \sigma(\omega_m^i, \omega_i) D(\omega_m^i)}{\sigma_t(\omega_i) \text{pdf}(\omega_m^i)},$$

*Research done when Yuang Cui was an intern at Nanjing University of Science and Technology.

†Corresponding author.

Authors' addresses: Gaole Pan, Nanjing University of Science and Technology, China, pangaole@njust.edu.cn; Yuang Cui, Anhui Science and Technology University, China, yuangcui@outlook.com; Jian Yang, Nanjing University of Science and Technology, China, csjyang@njust.edu.cn; Beibei Wang, Nanjing University, China, beibei.wang@nju.edu.cn.

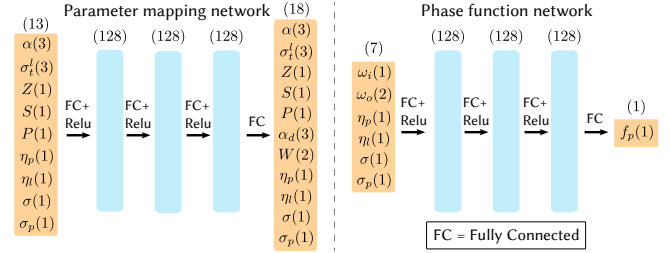


Fig. 1. The structures of two neural networks: the parameter mapping network (left) and the phase function network (right).

where N is the number of samples, and $\text{pdf}(\omega_m^i)$ is the probability density function (PDF) for the i -th sample. Specifically, the attenuation coefficients are stored as a 1D lookup table, parameterized by the polar angle θ of ω , while the phase function is stored as a 3D lookup table, with dimensions corresponding to the polar angle θ_i of ω_i , the polar angle θ_o of ω_o , and the azimuthal angle ϕ_o of ω_o , similar to the particle phase function table. In practice, we importance sample the normal distribution to improve the estimation efficiency.

1.2 WetSpongeCake

Neural network structure. The phase function network is a multi-layer perceptron (MLP) with three hidden layers, each containing 128 neurons, as shown in Fig. 1. Its input comprises phase function parameters and query directions, while its output is the phase function value. The parameter mapping network shares the same structure as the phase function network but differs in its input and output. Its input includes multiple scattering parameters. The output provides parameters for equivalent single scattering term, albedo α_d for the Lambertian term and the weights W for the two term.

Dataset. For the phase function network, we generate 6,000 phase functions by randomly sampling input parameters. Directions ω_i and ω_o are sampled using 64×64 uniform stratified samples. We use 90% of the dataset for training and reserve the remaining 10% for validation.

For the parameter mapping network, we generate 4,000 BSDFs by randomly sampling input parameters to create the training dataset. For each BSDF, we sample ω_i and ω_o using 32×32 uniform stratified samples. Starting from a sampled ω_i , Monte Carlo sampling is performed in the medium by repeatedly selecting a new position and a new direction based on the phase function. This process continues until the maximum depth of 10 is reached or the ray exits the

surface. For each ω_i , we trace 10,000 rays. Although the data contains noticeable noise, it does not affect the neural network training. The remaining configuration is consistent with the phase function network.

Training. The loss function for both two networks is the mean absolute error (MAE) between the ground truth and the network's output. Both the neural network and our single scattering model are implemented in the PyTorch framework, enabling automatic differentiation. We use the Adam optimizer with a learning rate of 0.001. The network is trained with a mini-batch size of 16. Phase function network took 1 hour and parameter mapping network took 4 hours training on an NVIDIA 3090 GPU.

2 DETAILED DERIVATION OF PARAMETER K

In this section, we present the derivation of K as outlined by Hapke [2008].

Hapke defined a porous medium where the porosity P represents the fraction of the volume not occupied by solid particles, n denotes the total number of particles per unit volume, and E is the extinction coefficient of the medium.

Assuming that all particles are significantly larger than the wavelength of light, equant, and randomly positioned and oriented, the mean particle volume is given as:

$$v = \frac{1-P}{n}. \quad (2)$$

Hapke conceptualized the medium as a lattice of imaginary cubes, each with edge length L , which represents the mean center-to-center distance between particles:

$$L = n^{-\frac{1}{3}}. \quad (3)$$

Given the random positioning of particles, the probability of light transmission through several layers is the product of the probabilities for each layer. Thus, the fraction of light remaining after traversing a distance t composed of $N = \frac{t}{L}$ layers is:

$$T(t) = (1-EL)^N = e^{N \ln(1-EL)} = e^{-KEt}, \quad (4)$$

where

$$K = -\frac{\ln(1-EL)}{EL}. \quad (5)$$

The mean geometric cross-sectional area of a particle is given by:

$$\sigma = \frac{E}{n}. \quad (6)$$

Assuming the particles are equant, that the diameter of a sphere with the same volume as a particle equals the diameter of a sphere with the same geometric cross-sectional area, we have:

$$D = \left(\frac{6}{\pi}v\right)^{\frac{1}{3}} = \left(\frac{4}{\pi}\sigma\right)^{\frac{1}{2}}. \quad (7)$$

Using the equations above, EL can be derived as follows:

$$\begin{aligned} EL &= n \frac{E}{n} L \\ &= n^{\frac{2}{3}} \frac{E}{n} \\ &= \left(\frac{1-P}{v}\right)^{\frac{2}{3}} \frac{\pi D^2}{4} \\ &= \left(\frac{1-P}{\frac{\pi D^3}{6}}\right)^{\frac{2}{3}} \frac{\pi D^2}{4} \\ &= \frac{(1-P)^{\frac{2}{3}}}{D^2 \left(\frac{\pi}{6}\right)^{\frac{2}{3}}} \cdot \frac{\pi D^2}{4} \\ &= \frac{\pi}{4 \cdot \left(\frac{\pi}{6}\right)^{\frac{2}{3}}} (1-P)^{\frac{2}{3}} \\ &= \left(\frac{3\sqrt{\pi}}{4} (1-P)\right)^{\frac{2}{3}}. \end{aligned} \quad (8)$$

Substituting Eqn. (8) into Eqn. (5), we obtain:

$$K = -\frac{\ln\left(1 - \left(\frac{3\sqrt{\pi}}{4} (1-P)\right)^{\frac{2}{3}}\right)}{\left(\frac{3\sqrt{\pi}}{4} (1-P)\right)^{\frac{2}{3}}}. \quad (9)$$

3 MORE RESULTS

In this section, we provide additional results as mentioned in our main paper. The parameter settings for the scenes presented in the main paper are detailed in Table 1.

Phase function visualization. We present a visualization of the phase function of the micro-ellipsoid model along with its corresponding mean cosine across different parameter settings in Fig. 2 and Fig. 3.

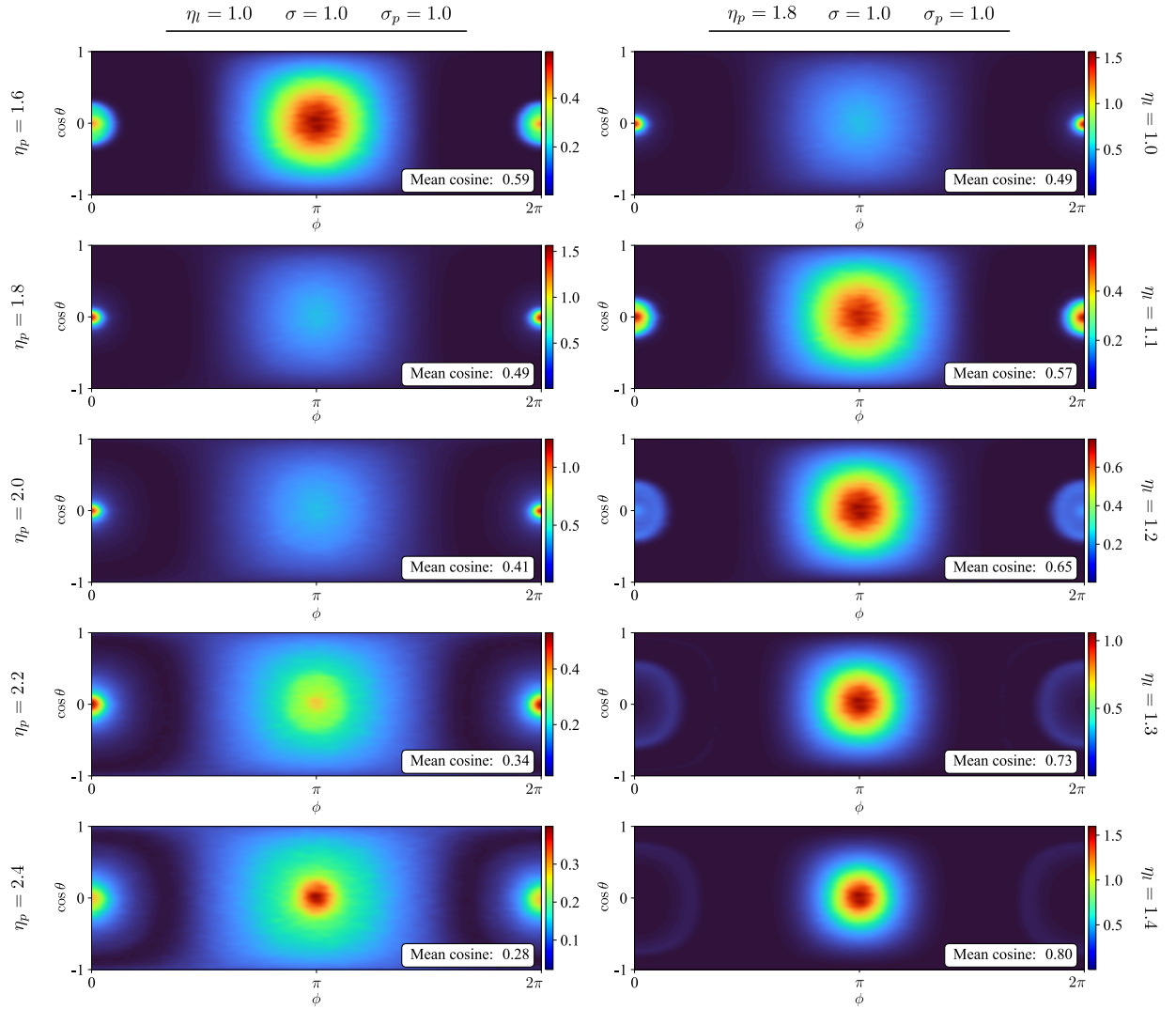
Parameter analysis. To demonstrate the impact of different parameters on appearance, we present renderings of the Sculpture scene under various parameter settings in Fig. 4. This scene is illuminated by two area light sources and an environment map.

REFERENCES

Bruce Hapke. 2008. Bidirectional reflectance spectroscopy: 6. Effects of porosity. *Icarus* 195, 2 (2008), 918–926. <https://doi.org/10.1016/j.icarus.2008.01.003>

Scene	Object	P	α	Z	S	σ_t^l	η_p	η_l	σ	σ_p
Sand	left	0.425	(0.88, 0.83, 0.71)	∞	0	(0, 0, 0)	2.1	1	1	1
	middle	0.425	(0.88, 0.83, 0.71)	∞	1	(0, 0, 0)	2.1	1.33	1	1
	right	0.425	(0.88, 0.83, 0.71)	∞	1	(1, 2, 2)	2.1	1.33	1	1
Cloth	cloth	1	(0.65, 0.09, 0.18)	4	map	(0, 0, 0)	2.4	1.33	0.1	0.1
Paper	paper	0.5	(0.88, 0.90, 0.92)	1	map	(0, 0, 0)	1.7	1.33	1	1
Table	table	0.5	map	∞	map	(0, 0, 0)	1.7	1.33	1	1
Teaser	pot (left)	0.5	map	∞	map	(0, 0, 0)	1.8	1.33	1	1
	pot (right)	0.5	map	∞	map	(1, 1, 1)	1.8	1.33	1	1
	cloth (white)	0.9	(0.7, 0.7, 0.7)	1.5	map	(0, 0, 0)	1.75	1.33	0.1	0.1
	cloth (red)	0.9	(0.7, 0.1, 0.1)	∞	map	(0, 0, 0)	2.4	1.33	0.1	0.1
	sculpture (left)	0.6	(0.85, 0.85, 0.85)	∞	map	(0, 0, 0)	1.8	1.33	1	1
	sculpture (right)	0.6	(0.85, 0.85, 0.85)	∞	map	(0, 0, 0)	1.8	1.501	1	1

Table 1. Parameters for different scenes and objects.

Fig. 2. Visualization of the phase function of the anisotropic micro-volume model along with its corresponding mean cosine, over varying refractive index of particle η_p and refractive index of liquid η_l .

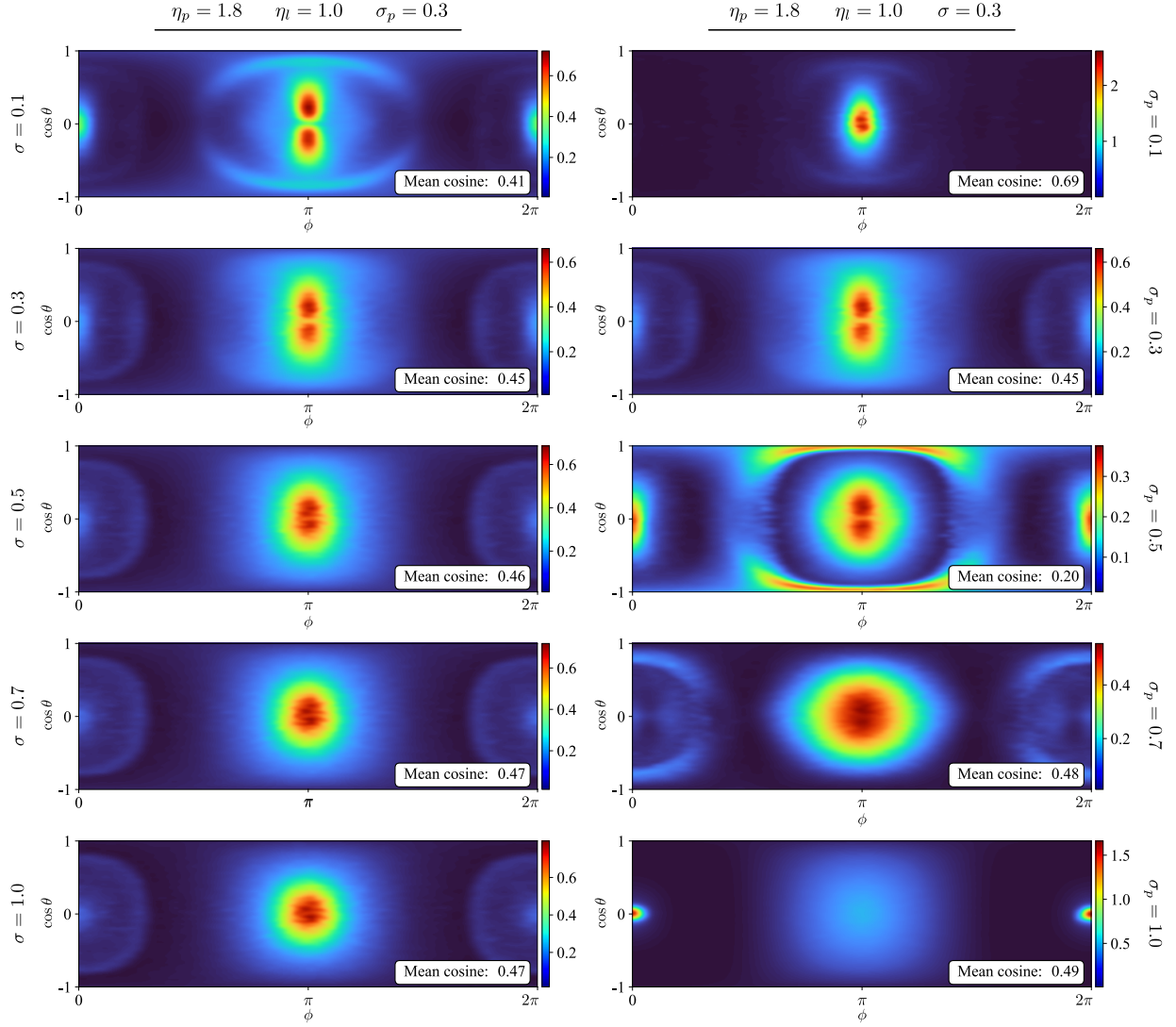


Fig. 3. Visualization of the phase function of the anisotropic micro-volume model along with its corresponding mean cosine, over varying normal projected area σ and particle projected area σ_p .

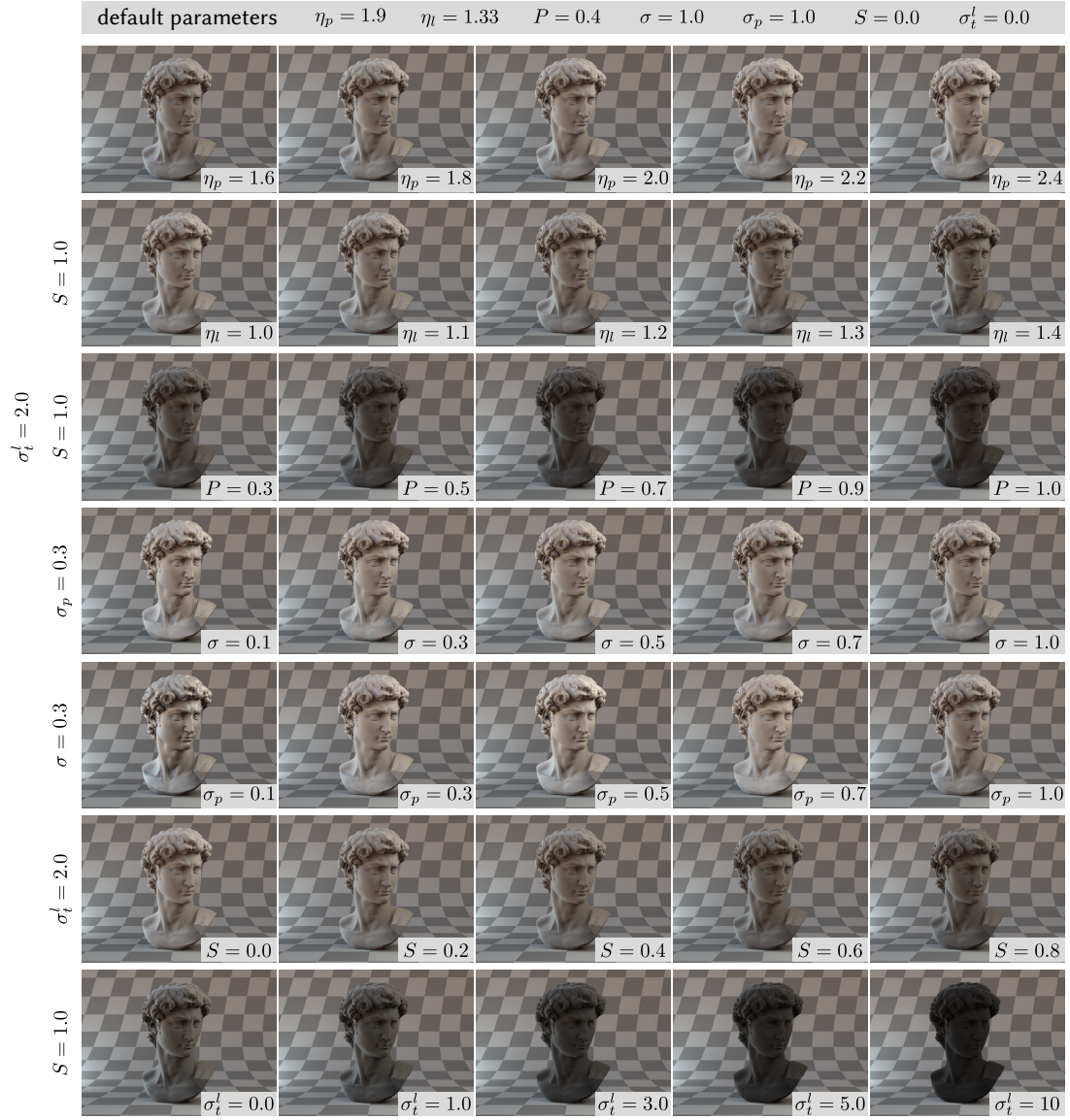


Fig. 4. Sculpture scene under different parameter settings. Parameters not explicitly mentioned are set to their default values, as indicated at the top of the figure.